Surface Deformation and Seismicity Induced by Poroelastic Stress at the Raft River Geothermal Field, Idaho, USA

Bing Q. Li[1†], Mostafa Khoshmanesh[2], Jean-Philippe Avouac[1]

[1] Division of Geological and Planetary Sciences, California Institute of Technology, CA, USA

[2] Department of Mechanical and Civil Engineering, California Institute of Technology, CA, USA

† Now at Department of Civil and Environmental Engineering, Western University, ON, Canada

Corresponding author: Bing Q. Li (bingqli@caltech.edu)

Key Points

- A hydro-mechanical model of effective stress changes from injection and production is calibrated using surface deformation from InSAR
- Seismicity, located predominantly in the basement, is primarily induced by poroelastic stress changes from cold water re-injection
- Similar stress changes trigger 4 time more earthquakes per unit volume in the basement than in the sedimentary cover.

Abstract

We investigate the relative importance of injection and production on the spatial-temporal distribution of induced seismicity at the Raft River geothermal field. We use time-series of InSAR measurements to document surface deformation and calibrate a hydro-mechanical model to estimate effective stress changes imparted by injection and production. Seismicity, located predominantly in the basement, is induced primarily by poroelastic stresses from cold water reinjection into a shallower reservoir. The poroelastic effect of production from a deeper reservoir is minimal and inconsistent with observed seismicity, as is pore-pressure-diffusion in the basement and along reactivated faults. We estimate an initial strength excess of ~20kPa in the basement and sedimentary cover, but the seismicity rate in the sedimentary cover is 4 times lower, reflecting lower density of seed-points for earthquake nucleation. Our modeling workflow could be used to assess the impact of fluid extraction or injection on seismicity and help design or guide operations.

Plain Language Summary

It is important to understand the mechanisms behind human-induced earthquakes, whether they are beneficial in the context of generating fractures for effective geothermal energy systems, or hazardous in the case of large earthquakes that may cause structural damage. Here, we present a case study of the Raft Rive geothermal field, which has operated since 2007 and generated earthquakes since 2010. Our objective is to understand how hot water, which is extracted from a deep sedimentary layer, and cold water, which is injected into a shallower layer, contribute to the observed seismicity, which have primarily occurred underneath the extraction layer. We construct a model to determine how the injection and extraction affect underground fluid pressures, and how these pressures impart stresses throughout the subsurface. This model is calibrated using InSAR, a satellite-based technique which

provides precise measurements the Earth's surface deformation in time. The results show that the shallow cold water injection is main culprit behind the deep earthquakes, because of the stresses imparted by the fluid pressure increase, whereas the effects of the deep extraction is negligible. Our modeling workflow could be used to assess the impact of fluid extraction or injection on seismicity and help guide operations.

1 Introduction

Injection and extraction of fluids from the subsurface can induce earthquakes (*e.g.*, Ellsworth, 2013). Induced seismicity can be intentional and beneficial. This is the case in the context of Enhanced Geothermal Systems where hydrofractures and shear-fractures are used to enhance permeability (Elsworth et al., 2016). In the context of CO2 storage, fracturing of the underburden, the rock volume beneath the target reservoir, could enhance the storage capacity. Most commonly though, seismicity is viewed as a source of hazard that can compromise the safe operation of a geothermal field or of a CO2 storage site (Zoback and Gorelick, 2012; Elsworth et al., 2016). In any case, there is much need for a better understanding of how such operations could induce earthquakes.

It is well established that the Coulomb Failure Stress change, ΔCFS, can be used to assess the risk of induced seismicity due to a stress change at a particular location (King et al., 1994; Stein, 1999). An increase of ΔCFS can in principle result from an increase of shear stress, an increase of pore pressure, or decrease of normal stress. In the case of fluid injection or extraction, ΔCFS at a given location might be due to pore pressure diffusion or due to thermo- or poroelastic stress changes (*e.g.*, Segall et al., 1994; Segall and Fitzgerald, 1998; Goebel and Brodsky, 2018). The effect of pressure diffusion might, in principle, be identified from the migration pattern of seismicity (*e.g.*, Shapiro et al.., 1997). By contrast, poroelastic stresses due to a well operation are imparted almost instantaneously and should result in a spatially stationary pattern which can reach large distances shortly after injection (Goebel et al, 2017;

Zhai and Shirzaei, 2019). In reality, disentangling the relative role of these mechanisms is often challenging. One reason is that the temporal evolution of seismicity also depends on the earthquake nucleation process, so that it does not reflect instantaneous stress changes (*e.g.*, Dieterich, 1994; Zhai and Shirzaei, 2019; Alghannam and Juanes, 2020). Another reason is that field operations often involve a complex set of injecting and extracting wells (*e.g.*, Hornbach et al., 2015); assigning seismicity to particular sources of stresses is therefore often ambiguous in such a context.

Here we study the case-example of seismicity induced at the Raft River geothermal field, which is particularly appropriate to gain insight into induced earthquake triggering mechanisms (Figure 1). The number of wells is relatively small and the geological setting is simple and well documented (*e.g.*, Bradford et al., 2013; Nash and Moore, 2012). In addition, a prominent geodetic signal has been previously observed using Synthetic Aperture Radar Interferometry, InSAR (Liu et al., 2018; Ali et al, 2018). Such measurements can indeed provide important constraints on the spatio-temporal evolution of the pressure field and fluid flow in the sub-surface reservoirs (Ali et al., 2018, Hoffmann et al., 2001; Chaussard et al., 2014). Finally, and most importantly for the purpose of this study, local seismic monitoring has revealed seismicity clearly correlated with the geothermal field (Figure 1a). One interesting specific feature of the raft River geothermal field is that hot water is produced from a ~100m thick reservoir at a depth of ~1500m below surface, and the cold water is reinjected in a distinct ~300m thick shallower reservoir at 500m depth below surface.

Given that the production reservoir directly overlies the seismogenic basement, it is unlikely that pore pressure diffusion into the basement is responsible for the observed seismicity. If the zone of seismicity were hydraulically connected to the reservoir, fluid extraction should have decreased the pore pressure, leading to fault strengthening. As a result, the thermo- and poroelastic contributions from production and injection are perhaps the primary mechanisms behind the induced seismicity. Hereafter, we first

give an overview of the setting of the Raft River geothermal field. We next present the methods used to model surface deformation and effective stress changes in the sub-surface. In the results section, we investigate the relative importance of injection and production on the spatial and temporal distribution of induced seismicity.

2 Setting of the Raft River Geothermal field

The Raft River geothermal site was identified in the 1950s, first developed as a DOE demonstration site in the 1970s, and significant production started by the end of 2007. The geology and geomechanical properties of the subsurface is relatively well documented in publicly available documents thanks to investigations conducted by the USGS and recent studies, and in relation to the recent EGS demonstration (Nash and Moore, 2012; Bradford et al., 2014, Bradford et al., 2015; Yuan et al, 2020). The Miocene to Pliocene sedimentary cover is about 1.5-2 km thick and consists of sub-horizontal interbedded volcanoclastics, volcanics, sandstones, and siltstones. It overlies a proterozoic metamorphic basement consisting of quartzite, schist and quartz monzonite. The area is part of the Basin-and-range zone of ~East-West active extension. Historical seismicity rates were however very low prior to production, with normal-faulting focal mechanisms broadly consistent with E-W extension (Zandt et al., 1982). Well logs show steeply dipping fractures trending approximately N-S (Bradford et al., 2013; Nash and Moore, 2012).

Hot water is extracted at a depth of ~1500m below surface from a ~100m thick quartzite layer through four wells (Figure 1b). One well, RRG-9 (Figure 1), was found to be poorly connected to the geothermal reservoir and selected for an Enhanced Geothermal System (EGS) stimulation. To avoid thermal drawdown, the cold water is injected through three wells into a shallower reservoir at a depth of approximately 500m below surface. This reservoir consists of Late Miocene tuff, about 300m thick.

In this study we used the baseline mechanical, hydrological, and poroelastic parameters of the reservoir rocks determined in previous hydro-thermal-mechanical studies (Liu et al., 2018; Yuan et al., 2020; Bradford et al., 2014) (Table 1). The reservoir permeability and compressibility were then calibrated to the geodetic data (Supplement 1) to better constrain the pore pressure diffusion and poroelastic stress change models respectively.

Significant production started only by the end of 2007 and ramped up gradually until 2010. The site was selected for an Enhanced Geothermal System (EGS) demonstration by DOE. The EGS demonstration was conducted at well RRG-9 over three phases between February 2012 and April 2014 with the goal of using hydraulic stimulation to improve the injectivity of the surrounding reservoir. Each phase consisted of cold fluid injection followed by a shut-in period to assess the pressure falloff characteristics. The well has since been used for continuous commercial use.

The Lawrence Berkeley National Laboratory deployed a local seismic network consisting of 10 stations which started operating in early 2010 (Supplementary Figure S2). Their seismicity catalog shows seismicity clearly clustered in the vicinity of the geothermal field, and correlated with the surface deformation pattern measured from InSAR (Figure 1a). Seismicity is located primarily in the metamorphic basement immediately underlying the production reservoir. It started in late 2010, lagging the onset of large-scale production by about 2 years and pre-dating the EGS stimulation. We note that the magnitude of completeness appears to decrease from $M_C \sim 0.5$ prior to the EGS stimulation, to $M_C \sim 0$ during and after the EGS stimulation. The seismicity cluster along a steeply dipping zone trending ~N60^{o}E which coincides with the Narrows Fault zone, a basement structure which had been inferred from geophysical and hydrological studies (Bradford et al., 2013; Dolenc et al., 1981).

3 Geomechanical Modelling

In our formulation, we account for the effects of pore pressure diffusion and its resultant poroelastic stress changes. We do not consider thermal effects given that the thermal contrasts are generally most important for injection of cold water, and the injection reservoir is very shallow (~500m depth) so that the poroelastic effects would dominate over the thermal effects as observed at the Salton Sea Geothermal Field in Southern California (Barbour et al., 2016). In the production reservoir, fluid extraction should only cause minor thermal effects as heat is advected horizontally, and so the horizontal temperature gradients should be small. This is corroborated by Liu et al's study (2018), where their coupled hydro-thermal-mechanical model of the Raft River geothermal field predicts that the poroelastic effects of fluid extraction and injection would dominate for the first 10 years, and the long-term effects of cooling in the injection reservoir would only emerge after 20 years of production.

In our workflow, we calculate the pressure change in the reservoir resulting from fluid injection and extraction, the surface displacements for comparison with the InSAR measurement, and the stresses in the basement and overlying sedimentary cover for comparison with the observed seismicity. We choose to employ analytical solutions here as they minimize the number of model parameters while providing an excellent fit to the geodetically measured surface deformation data. In addition, they are computationally inexpensive, which can enable, in principle, scaling to larger systems involving thousands of wells.

Given that the geology of the Raft River site can be generally considered as a vertically layered system (Liu et al., 2018), we employ a 2D axisymmetric model for pore pressure diffusion, where the pore pressure changes corresponding to production and injection can be considered separately in what we assume are unconnected reservoirs. In this formulation, considering a single well, the pore pressures at a given time, t, and a given location, $x = (x_1, x_2)$, from the well is,

151

$$P(x,t)=\frac{1}{H\,\rho_0\,4\pi\kappa}\int_0^t q(t')\frac{\exp\left[\frac{-r'^2}{4\,c(t-t')}\right]}{t-t'}dt' \quad (1)$$

152 where q(t') is the mass flow rate, c is the diffusivity, ρ_0 is the reference density, H is the thickness of the
153 layer, κ = k/η, k is the permeability, and η is the fluid viscosity. This solution is taken from Rudnicki
154 (1986), which we modified to allow anisotropy of the pore pressure diffusion, given that the surface
155 displacement (Figure 1a) suggests higher permeability in the ~N-S direction. The anisotropy is
156 implemented by transforming the radius r into an elliptical anisotropic radius r' defined as

$$r'=\frac{\xi\sqrt{x_1^2+x_2^2}}{\sqrt{\xi^2\sin^2(\theta-\varphi)+\cos^2(\theta-\varphi)}} \quad (2)$$

157 where ξ is the anisotropy factor, φ is the anisotropy angle of the direction of low permeability, and

158 $\theta=atan\left(\frac{x_2}{x_1}\right)$. The pressure changes are calculated independently for each injection and production
159 well, and superposed for all wells within the same reservoir.

160 Given the pore pressure distribution in the production and injection reservoirs, the induced poroelastic
161 stress and displacement fields can be approximated by gridding the pore pressure solution following
162 Kuvshinov (2008). The solutions for the entire stress tensor and displacement vector can be found in the
163 supplementary materials.

164 We evaluate the displacement at the surface (Supplement 1) and calibrate the model parameters using
165 the geodetic measurements. We also evaluate the stress changes in the basement and the sedimentary
166 cover in order to compare with seismicity. The stress changes are rotated to obtain normal and shear
167 components on a strike-slip fault oriented at N60°E with 76° dip corresponding to the Narrows fault

zone (Nash and Moore, 2012), and consistent with the orientation of the seismicity cluster. We calculate the Coulomb failure stress (CFS) change

$$\Delta CFS = \Delta\tau + \mu(\Delta\sigma_n + \Delta P), \quad (6)$$

where $\Delta\tau$ is the change in shear stress on the fault, $\Delta\sigma_n$ is the change in normal stress, ΔP is the change in pore pressure, and μ=0.6 is the friction coefficient.

4 Results

We use a volume rate of 0.1 m^3/s for injection wells, and 0.075 m^3/s for production wells following Liu et al. (2018), with a ramp-up time of two years. We also include the effect of the EGS injection at well RRG-9 ST1 (Figure 1) using the data reported in the thesis by Bradford (2016), discretized into monthly rates. To calibrate the model, we generate a range of model realizations for the surface displacement, and select the model parameters that minimize the misfit between the modelled and geodetically measured surface displacement. We vary the injection and production reservoir compressibility in the poroelasticity formulation continuously, and permeability in the pore pressure formulation discretely. We simulate 1 million instances of these parameters, and compare the 1D histogram of the modelled displacement at any given time sample with the corresponding measured displacement using the Wasserstein distance (Ramdas et al., 2017). We choose the Wasserstein distance as a goodness-of-fit criterion for the 1D histogram as it allows us to consider the distribution of positive and negative surface displacements while being insensitive to the exact spatial location of the bulb of uplift. The best-fit parameters for permeability and compressibility are given in Table 1. The uncertainty in the discretely sampled permeability is given as the width of the sampling bin, given that the best-fit value was preferred in all simulated instances. We determine the uncertainty for the continuously sampled compressibility parameter using a bootstrap method where we consider 100,000 subsamples of size 10,000 and select the best fitting model from each subsample. We then consider the 95% confidence

interval as the 2.5th and 97.5th percentile values from the population of best-fit compressibility values (Supplementary Figure S1), and how the uncertainty affects the CFS change.

Figure 1a shows the spatial distribution of vertical displacement rate averaged from 2007 to 2011, which shows a clear signal of uplift around the injection wells. These wells are injecting at 500m below the surface, and thus have a stronger signature across a smaller footprint compared to the production which occurs at a deeper depth of ~1.5 km below the surface. The elliptical bulb of uplift is well captured by our model (Figure 1b) estimated over the same time period of 2007 to 2011, which similarly shows highly localized uplift that is elongated in the NW-SE direction and generally captures the transition distance from uplift to subsidence. The isotropic model (Supplementary Figure S3) predicts an E-W elongated uplift pattern due to the distribution of wells that fails to match this feature. The elliptical shape of the zone of uplift is reproduced well by our pore pressure diffusion model thanks to the inclusion of anisotropy. The best-fitting permeability for the injection reservoir is 5.9 ± 1.5 x 10^{-13} m^2 in the direction of slow diffusion, which is trending N70°E, and 8.3 ± 2 x 10^{-13} m^2 in the direction of fast diffusion, which is trending N20°W. The N70°E permeability is within error from the value of 4.7 x 10^{-13} m^2 used by Liu et al. (2018), while the N20°W permeability indicates faster diffusion than predicted in their study. The permeability anisotropy is possibly due to the pre-existing fractures which are oriented ~N-S (Nash and Moore, 2012; Liu et al., 2018). The N20°E direction of fast diffusion and the anisotropy factor of 1.4 is also consistent with the analysis of Yuan et al., (2020), who found the permeability to be larger by a factor 1.2 to 2 along the NNE-SSW direction compared to the orthogonal direction.

Our model also reproduces the temporal behavior shown in Figure 1d, with an initial rapid uplift at location “A” before 2010, which then transitions to a steady-state with no further uplift. The seismicity is located within the general vicinity of the injection and production wells as shown in Figure 1, and begin in the basement in mid-2010 then continue in swarms of activity.

Figure 2a and 2b show the reservoir pressures resulting from injection and production respectively. As expected, these sources generate increased and decreased pore pressures in their respective reservoirs. Note that the effect of the stimulation of well RRG-9 is not visible due to the very small injection volume (Figure 3b). The resultant poroelastic stress changes in the basement, shown for April 2014 in Figure 2c and 2d for injection and production respectively, indicate that the poroelastic contributions to Coulomb failure stress (CFS) changes affect fault stability in the same manner as the pore pressures, i.e. injection causes increases in CFS due to both pore pressure and poroelastic effects, and vice versa for the production. As a result, the total CFS change in the basement (Figure 3a) suggests that injection is primarily responsible for the observed induced seismicity, which occur almost exclusively in the regions of positive CFS change. To explore the sensitivity to the assumed fault plane orientation, we test different receiver fault orientations and find that the zone of increased CFS change around the injection and production wells is largely unchanged. See Supplementary Figure S4 for the case of left-lateral and normal N-S faults parallel to regional documented faults (Nash and Moore, 2012).

The time evolution of CFS at the location of maximum uplift (point A) and the edge of the seismicity cloud (point B) suggests that the eastern edge of the seismicity is dominated entirely by stresses from the injection, while stresses on the western edge of the seismicity are inhibited significantly by the production (Figure 3c). Note that the pressure evolution at point B, located near well RRG-9, shows a very short-lived pressure increase. This figure also shows that although the simulation assumes a simple ramp to constant flow rate from 2008 to 2010, the zone of Coulomb stress increase due to poroelastic loading of the basement keeps increasing until the end of the simulation as the zone of high pore pressure in the shallow reservoir expands away from the injection wells. This can explain the sustained seismic activity. Additionally, the CFS change at “A” as shown in Figure 3c indicates there may be a critical Coulomb stress increase of approximately 50kPa required to trigger the seismicity. That would represent the initial strength excess, i.e. the initial distance from the failure criterion, within the

Narrows fault zone. To further investigate this, we calculate the CFS change at the specific origin time and hypocentral location of the observed earthquakes (Figure 4a). In this calculation we assume the same hypocentral depth of 500m for events in the basement, and -500m for events in the overlying sedimentary cover. We can see that nucleation stresses range from 0 to 70kPa for events in the basement and the overlying sedimentary cover, and the histograms shown in Figure 4b and 4c show a possibly bimodal distribution of nucleation stress for the basement with a main mode at 19kPa. It is interesting that the two histograms are actually quite similar despite the fact that very few earthquakes occurred in the sedimentary cover. According to our analysis a given volume of basement rocks submitted to a given ΔCFS produces 4 times more earthquakes than the same volume of sedimentary rocks submitted to the same ΔCFS. This is because the earthquake productivity, representing the density of possible nucleation points of earthquake with magnitude larger than the detection threshold, must be 4 times larger in the basement than in the sedimentary cover (Figure 4d).

Given the magnitude of the pore pressure changes in the production reservoir, which are about 100 times larger than the magnitude of the poroelastic stress changes, we believe it is justified to consider the production reservoir to be uncoupled from the basement, otherwise we would not expect any seismicity whatsoever since the pore pressure reduction from extraction would completely dominate the state of stress in the basement. We account for the hydraulic stimulation at RRG-9-ST1 as an additional injection well located in the production reservoir, although we note that its corresponding pore pressure contributions are small relative to the standard production wells given the low injection volumes (Figure 3b). This can be seen in the stress changes at point “B” (Figure 3c), which is located close to well RRG-9 but only experiences small stress changes on the order of ~1kPa as a result of the stimulation at the well. Considering the spatial distribution of seismicity prior to the first stimulation phase, we see that the majority of the central seismicity cloud is already activated before March 2012 even with the lower magnitude of completeness (Supplementary Figure S2), and so the hydraulic

stimulations likely did not significantly affect the hydraulic connection between the basement and the production reservoir. This is supported by the observation that we do not generally see spatial diffusion of earthquake events away from well RRG-9 after the three stimulation events (Supplementary Figure S2c).

5 Discussion and Conclusions

Together with previous studies which have adopted a similar strategy (Juanes et al., 2016; Shirzaei et al., 2016), our study demonstrates the value of combining observation of surface deformation and simple fluid flow and geomechanical modeling to analyze induced seismicity due to injection and extraction of fluids from the subsurface. We acknowledge that our evaluation of uncertainties incorporates only the sensitivity of our analytical solution, and does not account for potential sources of correlated error in the InSAR measurements (*e.g.* tropospheric corrections, ionospheric effects) or epistemic uncertainties relating to our assumption of homogeneous reservoir properties in a homogeneous elastic half-space. Nevertheless, we believe that our main findings, at least qualitatively, are not dependent on these uncertainties, given the similarity of our modelled and measured surface displacements with previous works (Liu et al., 2018; Ali et al., 2018), as well as our ability to resolve the permeability anisotropy suggested by Yuan et al. (2020).

The spatial distribution of ΔCFS contributions (Figs 2c, 2d) in the basement strongly suggest that poroelastic stress changes from shallow injection is responsible for the timing and location of observed induced seismicity. The pore pressures from injection are not connected to the basement and the poroelastic stress changes resulting from fluid extraction are smaller in magnitude compared to the injection. Figure 3a, which shows the net ΔCFS in the basement, indicates that all earthquake events occur in the region of positive slip potential, which suggests that while the magnitude of the contribution from production is small, it nevertheless has an inhibiting effect on fault slip potential, for

284 example in the region to the north of well RRG-9 ST1. In terms of the distribution of ΔCFS at the time
285 and location of earthquake nucleations (Figure 4), we also find that the basement has an initial strength
286 excess of approximately 15 – 20kPa, and an excess of 20 – 25kPa in the overlying sedimentary cover
287 which is required to activate the fault, similar to the observations at Groningen by Smith (2019).

288 In terms of the timing of seismicity in relation to the DOE hydraulic fracturing project at well RRG-9 ST1,
289 our results show that the seismicity begins in late 2010 whereas the first phase at well RRG-9 ST1 begins
290 in early 2012. This, in conjunction with the minimal CFS changes at "B" (located close to well RRG-9 ST1)
291 in Figure 3c, show that while the project did indeed trigger some induced events (Bradford, 2016), the
292 timing and location nevertheless correspond to the larger-scale spatial distribution of CFS change shown
293 in Figure 3a.

294 Overall, our results show that the observed spatial and temporal distribution of surface deformation and
295 induced seismicity at the Raft River geothermal site may be reasonably explained by simple analytical
296 solutions for axisymmetric pore pressure diffusion and its resultant poroelastic stress changes. Our
297 model uses only a simplified 1D geological model as well as injection and production rates as inputs,
298 where geomechanical parameters are constrained by fitting the modelled surface displacement to the
299 true surface displacement as observed by InSAR measurements. This simple framework is scalable and
300 easily calibrated given the small number of parameters, and can be readily applied to investigate large
301 multi-well systems involving combined injection and production such as Oklahoma and Texas
302 (Langenbruch and Zoback, 2016; Zhai et al., 2018; Walter et al., 2018), where existing studies are
303 primarily focused on the effects of fluid injection. Our framework may be used to inform geothermal
304 and carbon storage strategies, where the seismicity in the basement and elsewhere could in principle be
305 controlled by regulating the injection rates (Kwiatek et al., 2019; Birkholzer et al., 2012; Cihan et al.,
306 2015). We conjecture that, using the modeling workflow presented in this study, the location and time-

307 evolution of seismicity induced by fluid extraction could in principle be controlled by adjusting well flow
308 rates.

Acknowledgements

The authors declare no competing interests. ALOS data set are obtained through Alaska Satellite Facilities at https://vertex.daac.asf.alaska.edu/, and the seismicity catalogue was downloaded from the Lawrence Berkeley National Laboratory at http://esd.lbl.gov/research/projects/induced_seismicity/egs/raft_river.html. This study was supported by the NSF/ IUCRC Geomechanics and Mitigation of Geohazards (National Science Foundation award #1822214). We thank Jonny Smith for discussions and help de-bugging.

References

Alghannam, M. & Juanes, R., 2020. Understanding rate effects in injection-induced earthquakes, *Nature Communications*, 11.

Ali, S.T., Reinisch, E.C., Moore, J., Plummer, M., Warren, I., Davatzes, N.C., Feigl, K.L. (2018) Geodetic measurements and numerical models of transient deformation at Raft River geothermal field, Idaho, USA. *Geothermics*, 74, 106-111, doi: 10.1016/j.geothermics.2018.02.007

Barbour, A.J., Evans, E.L., Hickman, S.H., Eneva, M. (2016) Subsidence rates at the southern Salton Sea consistent with reservoir depletion. *Journal of Geophysical Research: Solid Earth*, 121, 5308–5327, doi:10.1002/2016JB012903

Birkholzer, J.T., Cihan, A. & Zhou, Q., 2012. Impact-driven pressure management via targeted brine extraction-Conceptual studies of CO2 storage in saline formations, *International Journal of Greenhouse Gas Control*, 7, 168-180.

Bourne, S.J., Oates, S.J., van Elk, J., Doornhof, D. (2014) A seismological model for earthquakes induced by fluid extraction from a subsurface reservoir. *Journal of Geophysical Research*: *Solid Earth*, 119(12), 8991-9015, doi: 10.1002/2014JB011663

Bourne, S.J. & Oates, S.J., 2017. Extreme Threshold Failures Within a Heterogeneous Elastic Thin Sheet and the Spatial-Temporal Development of Induced Seismicity Within the Groningen Gas Field, *Journal of Geophysical Research-Solid Earth*, 122, 10299-10320.

Bradford, J.T. (2016) The Application of Hydraulic and Thermal Stimulation Techniques to Create Enhanced Geothermal Systems (Doctoral Dissertation)

Bradford, J., McLennan, J., Moore, J., Glasby, D., Waters, D., Kruwell, R., Bailey, A., Rickard, W., Bloomfield, K., King, D. (2013) Recent developments at the Raft River geothermal field. In: *Proceedings of the 38th workshop on geothermal reservoir engineering*, Stanford, CA 2013

Bradford, J., McLennan, J., Moore, J., Podgorney, R., Tiwari, S. (2015) Hydraulic and Thermal Stimulation Program at Raft River Idaho, A DOE EGS. *Geothermal Resources Council Transactions*, 39, 261-268.

Bradford, J.T., Ohren, M., Osborn, W.L., McLennan, J., Moore, J., Podgorney, R. (2014) Thermal Stimulation and Injectivity Testing at Raft River, ID EGS Site. *PROCEEDINGS, Thirty-Ninth Workshop on*

Geothermal Reservoir Engineering Stanford University, Stanford, California, February 24-26, 2014 SGP-TR-202

Chaussard, E., Burgmann, R., Shirzaei, M., Fielding, E.J. & Baker, B., 2014. Predictability of hydraulic head changes and characterization of aquifer-system and fault properties from InSAR-derived ground deformation, *Journal of Geophysical Research: Solid Earth*, 119, 6572-6590.

Cihan, A., Birkholzer, J.T. & Bianchi, M., 2015. Optimal well placement and brine extraction for pressure management during CO2 sequestration, *International Journal of Greenhouse Gas Control*, 42, 175-187.

Dieterich, J.H., 1994. A constitutive law for the rate of earthquake production and its application to earthquake clustering, *J. Geophys. Res*., 99, 2601-2618.

Dolenc, M. R., Hull, L. C., Mizell, S. A., Russell, B. F., Skiba, P. A., Strawn, J. A., et al. (1981). Raft River geoscience case study. (EGG-2125). Idaho Falls, Idaho: EG&G, Idaho, Inc.

Elsworth, D., Fang, Y., Gan, Q., Im, K. J., Ishibashi, T., & Guglielmi, Y. (2016). Induced seismicity in the development of EGS—benefits and drawbacks. In H. Li, J. Li, Q. Zhang, & J. Zhao (Eds.), *Rock Dynamics: From Research to Engineering - 2nd International Conference on Rock Dynamics and Applications, ROCDYN 2016* (pp. 13-24). CRC Press/Balkema. doi:10.1201/b21378-4

Ellsworth, W. (2013) Injection-Induced Earthquakes. *Science*, 341(6142). doi: 10.1126/science.1225942

Farr, T. G., Rosen, P. A., Caro, E., Crippen, R., Duren, R., Hensley, S., et al. (2007). The shuttle radar topography mission. *Reviews of Geophysics*, *45*(2), Rg2004. doi: 10.1029/2005rg000183

Franceschetti, G., & Lanari, R. (1999). *Synthetic aperture radar processing*. Boca Raton, Florida: CRC Press.

Goebel, T.H.W. & Brodsky, E.E. (2018) The spatial footprint of injection wells in a global compilation of induced earthquake sequences. *Science*, 361(6405), 899-904, doi: 10.1126/science.aat5449

Goebel, T.H.W., Weingarten, M., Chen, X., Haffener, J. & Brodsky, E.E., 2017. The 2016 Mw5.1 Fairview, Oklahoma earthquakes: Evidence for long-range poroelastic triggering at > 40 km from fluid disposal wells, *Earth and Planetary Science Letters*, 472, 50-61.

Goertz-Allman, B.P., Gibbons, S.J., Oye, V., Bauer, R., Will, R. (2017) Characterization of induced seismicity patterns derived from internal structure in event clusters. *Journal of Geophysical Research: Solid Earth*, 122(5), 3875-3894, doi: 10.1002/2016JB013731

Hooper, A., & Zebker, H. A. (2007). Phase unwrapping in three dimensions with application to InSAR time series. *J. Opt. Soc. Am. A.*, *24*(9).

Hoffmann, J., Zebker, H.A., Galloway, D.L. & Amelung, F., 2001. Seasonal subsidence and rebound in Las Vegas Valley, Nevada, observed by synthetic aperture radar interferometry, *Water Resources Research*, 37, 1551-1566.

Hornbach, M.J., DeShon, H.R., Ellsworth, W.L., Stump, B.W., Hayward, C., Frohlich, C., Oldham, H.R., Olson, J.E., Magnani, M.B., Brokaw, C., Luetgert, J.H. (2015). Causal factors for seismicity near Azle, Texas. *Nature Communications*, 6, doi: 10.1038/ncomms7728

Ito, T. & Zoback, M.D., 2000. Fracture permeability and in situ stress to 7 km depth in the KTB Scientific Drillhole, *Geophysical Research Letters*, 27, 1045-1048.

Juanes, R., Jha, B., Hager, B.H., Shaw, J.H., Plesch, A., Astiz, L., Dieterich, J.H. & Frohlich, C., 2016. Were the May 2012 Emilia-Romagna earthquakes induced? A coupled flow-geomechanics modeling assessment, *Geophysical Research Letters*, 43, 6891-6897.

King, G.C.P., Stein, R.S. & Lin, J., 1994. Static Stress Changes and The Triggering Of Earthquakes, *Bulletin Of The Seismological Society Of America*, 84, 935-953.

Kuvshinov, B.N. (2008) Elastic and piezoelectric fields due to polyhedral inclusions. *International Journal of Solids and Structures*,45(5), 1352-1384, doi: 10.1016/j.ijsolstr.2007.09.024

Kwiatek, G., Saarno, T., Ader, T., Bluemle, F., Bohnhoff, M., Chendorain, M., Dresen, G., Heikkinen, P., Kukkonen, I., Leary, P., Leonhardt, M., Malin, P., Martinez-Garzon, P., Passmore, K., Pasmore, P., Valenzuela, S., Wollin, C. (2019) Controlling fluid-induced seismicity during a 6.1-km-deep geothermal stimulation in Finland. *Science Advances*, 5(5), doi: 10.1126/sciadv.aav7224

Langenbruch, C. & Zoback, M.D. (2016) How will induced seismicity in Oklahoma respond to decreased saltwater injection rates? *Science Advances*, 2(11), doi: 10.1126/sciadv.1601542

Lawrence Berkeley Induced Seismicity EGS. Interactive, Map of Earthquakes at Raft River. http://esd.lbl.gov/research/projects/induced_seismicity/egs/raft_river.html (accessed April, 2021).

Liu, F., Fu, P., Mellors, R.J., Plummer, M.A., Ali, S.T., Reinisch, E.C., Liu, Q., Feigl, K.L. (2018) Inferring Geothermal Reservoir Processes at the Raft River Geothermal Field, Idaho, USA, Through Modeling InSAR–Measured Surface Deformation. *Journal of Geophysical Research: Solid Earth*, 123(5), 3645-3666, doi: 10.1029/2017JB015223

Lopez-Martinez, C., & Fabregas, X. (2002). Modeling and reduction of SAR interferometric phase noise in the wavelet domain. *Ieee Transactions on Geoscience and Remote Sensing*, *40*(12), 2553-2566. doi: 10.1109/TGRS.2002.806997

Mignan, A., Landtwing, D., Kastli, P., Mena, B., Wiemer, S. (2015) Induced seismicity risk analysis of the 2006 Basel, Switzerland, Enhanced Geothermal System project: Influence of uncertainties on risk mitigation. *Geothermics*, 53, 133-146, doi: 10.1016/j.geothermics.2014.05.007

Nash, G.D. & Moore, J.N. (2012) Raft River EGS Project A GIS Centric Review of Geology. *Geothermal Resources Council Transaction*s, 36, 951-958.

Ramdas, A., Trillos, N.G., Cuturi, M. (2017) On Wasserstein Two-Sample Testing and Related Families of Nonparametric Tests. *Entropy*, 19(2), doi: 10.3390/e19020047

Rudnicki, J.W. (1986) Fluid mass sources and point forces in linear elastic diffusive solids. *Mechanics of Materials*, 5(4), 383-393

Segall, P., Grasso, J.R. & Mossop, A., 1994. Poroelastic stressing and induced seismicity near the Lacq gas-field, southwestern France, *Journal of Geophysical Research: Solid Earth*, 99, 15423-15438.

Segall, P. & Fitzgerald, S.D., 1998. A note on induced stress changes in hydrocarbon and geothermal reservoirs, *Tectonophysics*, 289, 117-128.

Shapiro, S.A., Huenges, E. & Borm, G., 1997. Estimating the crust permeability from fluid-injection-induced seismic emission at the KTB site, *Geophysical Journal International*, 131, F15-F18.

Shirzaei, M. (2013). A Wavelet-Based Multitemporal DInSAR Algorithm for Monitoring Ground Surface Motion. *IEEE Geoscience and Remote Sensing Letters*, *10*(3), 456-460. doi: 10.1109/Lgrs.2012.2208935

Shirzaei, M., & Bürgmann, R. (2012). Topography correlated atmospheric delay correction in radar interferometry using wavelet transforms. *Geophysical Research Letters*, *39*(1), L01305. doi: 10.1029/2011GL049971

Shirzaei, M., & Bürgmann, R. (2013). Time-dependent model of creep on Hayward fault inferred from joint inversion of 18 years InSAR time series and surface creep data. *Journal of Geophysical Research-Solid Earth*, *118*, 1733–1746. doi: 10.1002/jgrb.50149

Shirzaei, M., Ellsworth, W.L., Tiampo, K.F., Gonzalez, P.J. & Manga, M., 2016. Surface uplift and time-dependent seismic hazard due to fluid injection in eastern Texas, *Science*, 353, 1416-1419.

Shirzaei, M., & Walter, T. R. (2011). Estimating the Effect of Satellite Orbital Error Using Wavelet-Based Robust Regression Applied to InSAR Deformation Data. *Ieee Transactions on Geoscience and Remote Sensing*, *49*(11), 4600-4605. doi: 10.1109/Tgrs.2011.2143419

Smith, J. D. (2019). Geomechanical properties of the Groningen reservoir (doctoral thesis). doi: 10.17863/CAM.41005

Stein, R.S., 1999. The role of stress transfer in earthquake occurrence, *Nature*, 402, 605-609.

Stork, A.L., Verdon, J.P., Kendall, J.-M. (2015) The microseismic response at the In Salah Carbon Capture and Storage (CCS) site. *International Journal of Greenhouse Gas Control*, 32, 159-171, doi: 10.1016/j.ijggc.2014.11.014

Tan, Y., Hu, J., Zhang, H., Chen, Y., Qian, J., Wang, Q., Zha, H., Tang, P., Nie, Z. (2020) Hydraulic Fracturing Induced Seismicity in the Southern Sichuan Basin Due to Fluid Diffusion Inferred From Seismic and Injection Data Analysis. *Geophysical Research Letters*, 47(4). doi: 10.1029/2019GL084885

Walter, J.I., Frohlich, C., Borgfeldt, T. (2018) Natural and induced seismicity in the Texas and Oklahoma Panhandles. *Seismological Research Letters*, 89(6), 2437-2446, doi: doi.org/10.1785/0220180105

Yuan, Y.L., Xu, T.F., Moore, J., Lei, H.W. & Feng, B., 2020. Coupled Thermo-Hydro-Mechanical Modeling of Hydro-Shearing Stimulation in an Enhanced Geothermal System in the Raft River Geothermal Field, USA, *Rock Mechanics and Rock Engineering*, 53, 5371-5388.

Zandt, G, McPherson, L, Schaff, S, & Olsen, S. Seismic baseline and induction studies: Roosevelt Hot Springs, Utah and Raft River, Idaho. *United States*. doi:10.2172/6396329

Zhai, G. & Shirzaei, M. (2018). Fluid Injection and Time−Dependent Seismic Hazard in the Barnett Shale, Texas. *Geophysical Research Letters*, 45(10), 4743-4753. doi: 10.1029/2018GL077696

Zhai, G., Shirzaei, M., Manga, M., Chen, X. (2019). Pore-pressure diffusion, enhanced by poroelastic stresses, controls induced seismicity in Oklahoma. *Proceedings of the National Academy of Sciences*, 116 (33), 16228-16233. doi: 10.1073/pnas.1819225116

453 Zoback, M.D. & Gorelick, S.M., 2012. Earthquake triggering and large-scale geologic storage of carbon
454 dioxide, *Proceedings of the National Academy of Sciences of the United States of America*, 109, 10164-
455 10168. doi: 10.1073/pnas.1202473109

Tables and Figures

Table 1: Hydro-and geomechanical properties used for simulation of pore pressures and poroelastic stress changes. The parameters which are calibrated using the surface deformation measurements are shown in bold. The values in parentheses indicate a priori values, and uncertainties at the 95% confidence level are estimated from bootstrap sampling (Supplementary Figure S1).

	Injection Reservoir	Production Reservoir	Narrows Fault
Fluid density ρ, (kg/m^3)	998	998	
Fluid viscosity, (Pa s)	8.9 x 10^{-4}	8.9 x 10^{-4}	
Skempton's coefficient, B	0.75	0.75	
Permeability, k (m^2)	**5.9 ± 1.5 x 10^{-13}** (4.7 x 10^{-13})	**5 ± 1.3 x 10^{-13}** (4 x 10^{-13})	
Porosity	0.15	0.15	
Compressibility, C_m (Pa^{-1})	**6.1 ± 0.3 x 10^{-9}** (5.1 x 10^{-9})	**2.5 ± 0.4 x 10^{-10}** (2.04 x 10^{-9})	
Shear modulus, μ (GPa)	0.833	2.08	
Thickness, (m)	300	100	
Biot coefficient, α	0.31	0.31	
Poisson's ratio, ν	0.2	0.2	
Flow anisotropy factor, ξ	1.4	1.4	
Flow anisotropy angle, φ	20° (slow diffusion N70°E)	20° (slow diffusion N70°E)	
Friction angle, (°)			31
Strike, (°)			N60°E
Dip, (°)			76
Sense			Sinistral

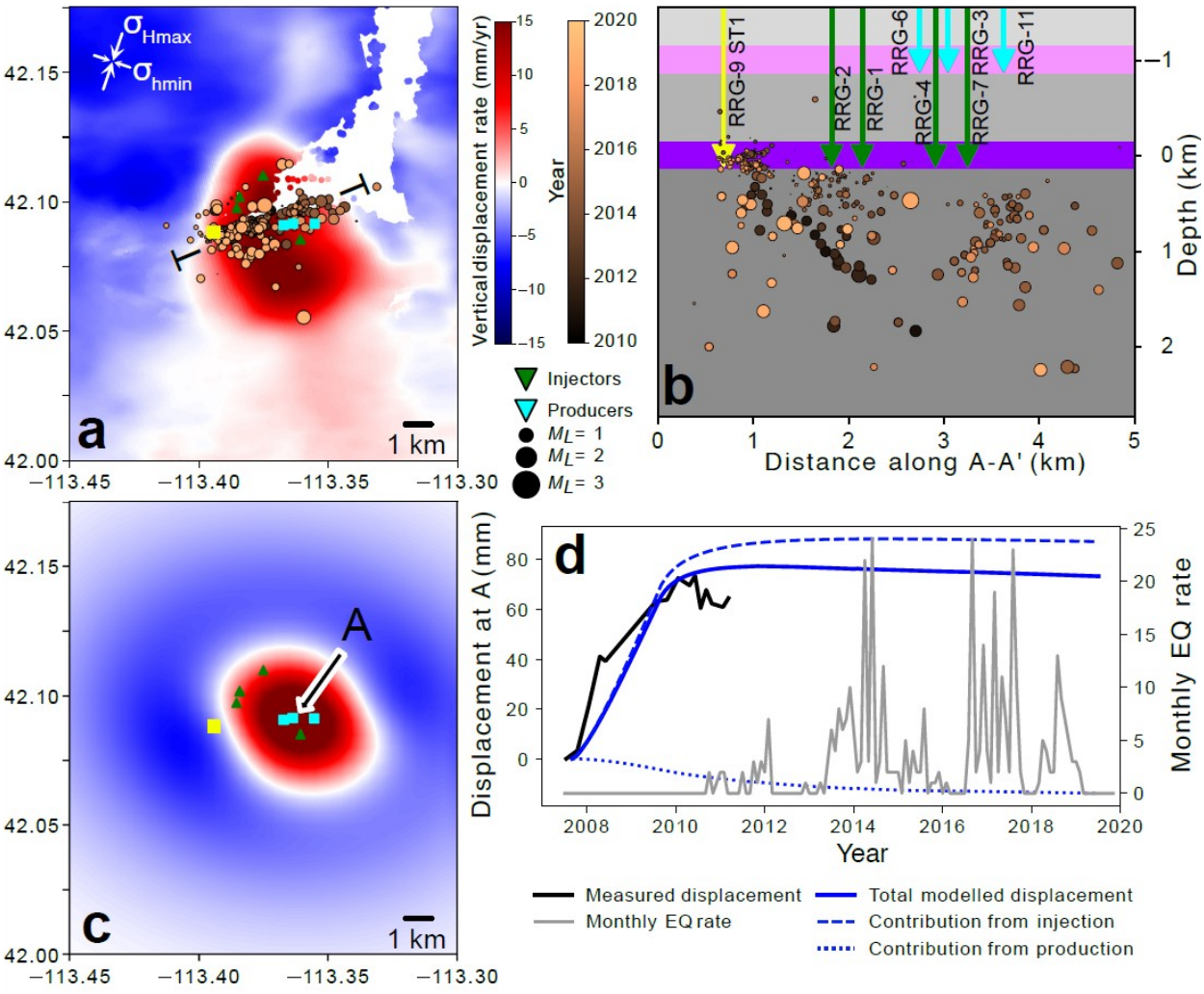

Figure 1: Summary showing a) the geodetically measured surface displacement rate during 2007-2011, location of injection and production wells, and detected earthquakes; b) southeast-northwest depth cross section of simplified site geology, showing well and earthquake locations; c) modelled surface displacement rate; d) time evolution of seismicity rate and measured and modelled surface displacements at point "A". DOE experimental well RRG-9, which is injecting into the production reservoir, is shown in the yellow square. Vertical displacement referenced as positive upwards, depths referenced to sea level. EQ = Earthquake.

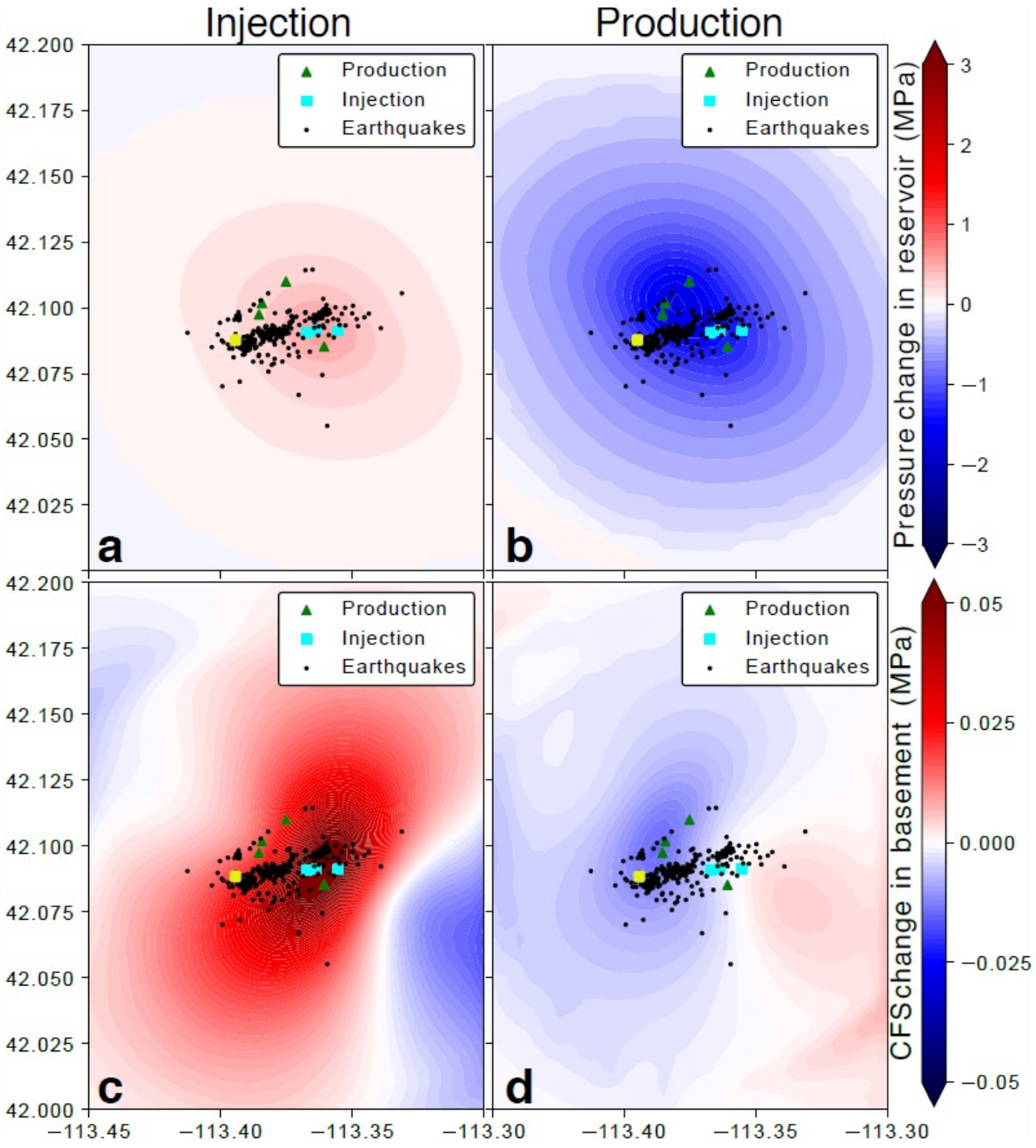

Figure 2: Spatial maps of pressure change in the reservoirs in April 2014 corresponding to a) injection, b) production; and Coulomb failure stress (CFS) changes in the basement attributed to c) injection and d) production, calculated on a steeply dipping left-lateral N60E fault.

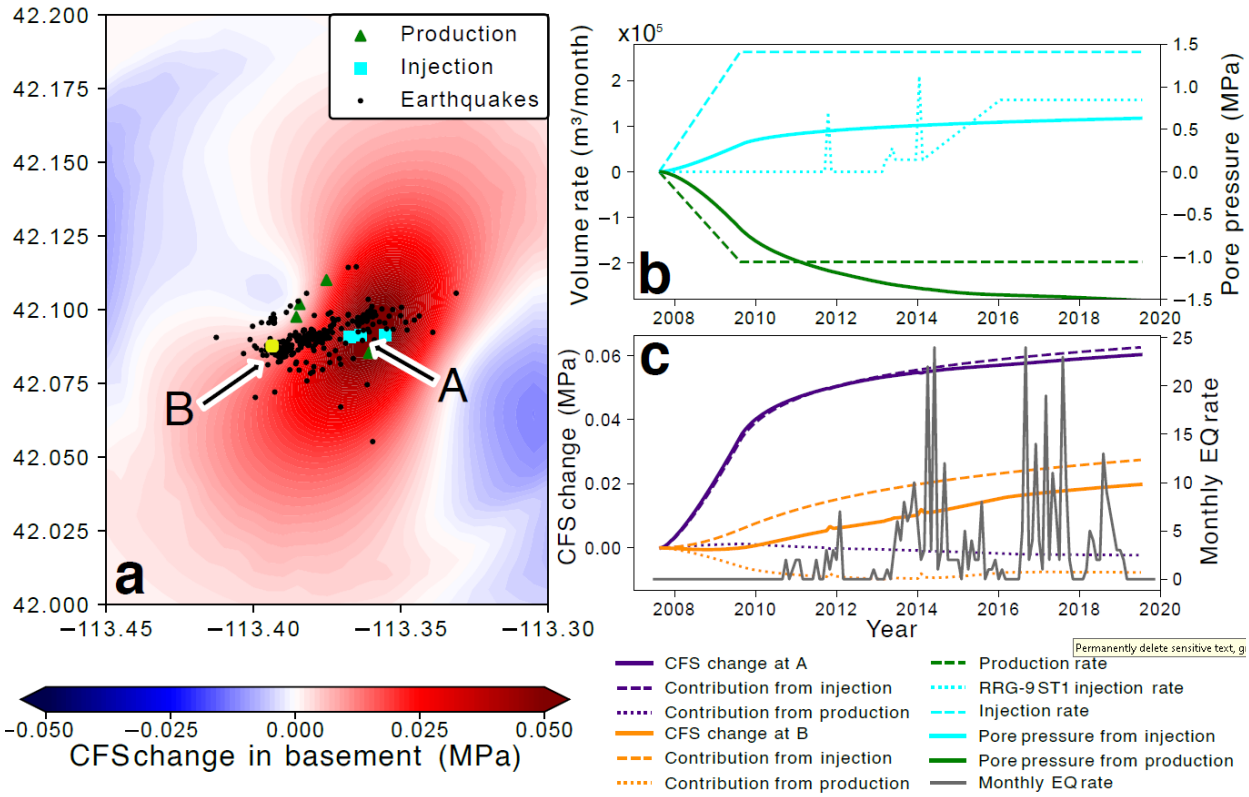

Figure 3: Modelled Coulomb failure stress (CFS) changes in the basement due to the combined effects of injection and production. a) shows the spatial distribution of CFS in the basement in April 2014, b) shows the imposed volume rates, c) shows the modelled CFS change at points "A" and "B" (Figure 1b) in the basement over time, alongside the measured seismicity rate.

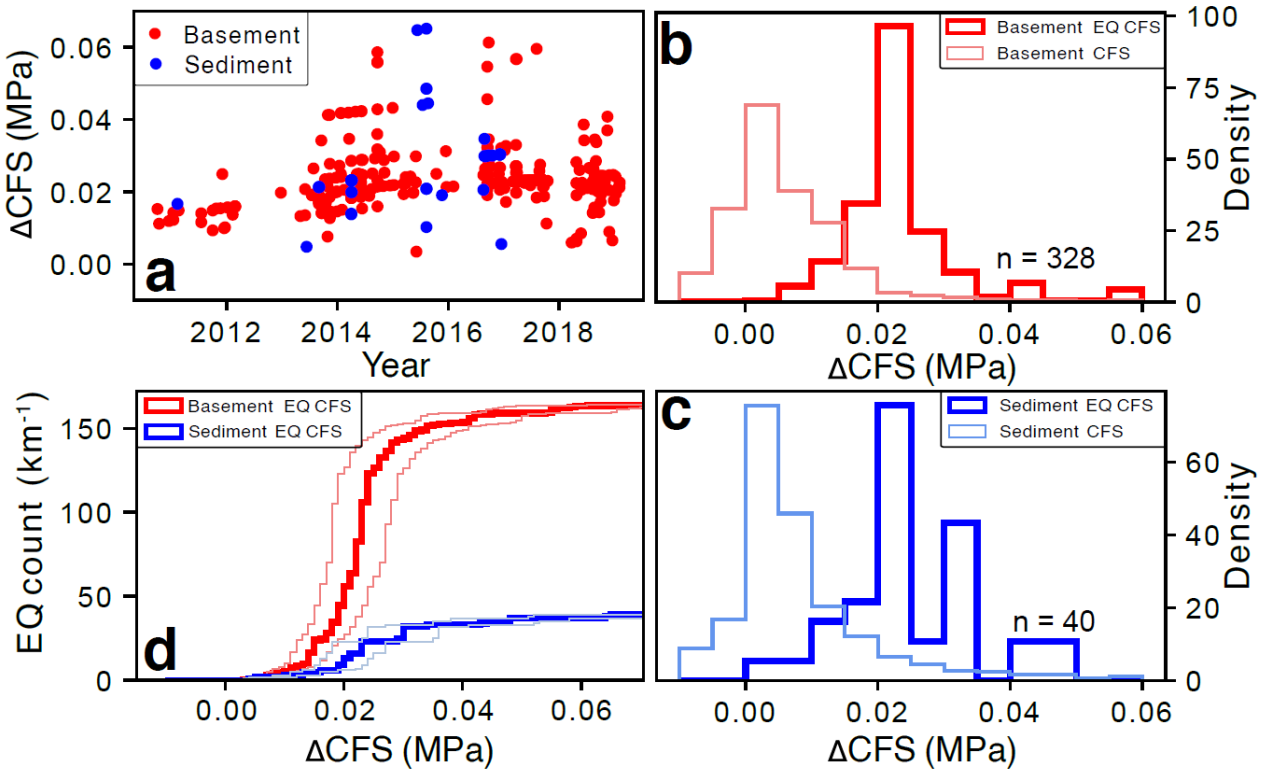

Figure 4: Coulomb failure stress (CFS) at time and location of detected earthquakes, a) shown over time for events detected in the basement and the overlying sedimentary cover. b) and c) show the histograms of the CFS at earthquake nucleation compared to the overall distribution of CFS in the basement and sedimentary cover formation respectively. d) Cumulative histogram of CFS at earthquake nucleation for the basement and the sedimentary cover, normalized by the thickness of the activated rock (1km for sediment, 2km for basement). Light coloured lines indicate 95% confidence intervals estimated according to bootstrap sampling (Supplementary Figure S1). EQ = Earthquake.

Supplement 1 - Spatio-temporal evolution of surface deformation

Following on previous studies (Ali et al., 2018; Liu et al.), we use Interferometric Synthetic Aperture Radar (InSAR) to measure the time evolution of surface deformation associated with the geothermal operations at the Raft River site. To this end, we use a wavelet-based multitemporal InSAR algorithm, so-called WabInSAR (Shirzaei, 2013; Shirzaei & Bürgmann, 2013), applied to a time series of L-band SAR images. The data set is comprised of 17 Level 1.0 Single-Look Complex (SLC) images acquired by ALOS PALSAR in the ascending path #204 and frame #830, spanning 6/13/2007 to 2/6/2011. To reduce the effect of speckle noise, SLCs are multilooked with a factor of 10 and 16 along the range and azimuth, respectively, generating pixels with size of 47m × 50m. All the SLCs are then accurately coregistered to a single reference image, which is chosen in a way that minimizes the total spatiotemporal baseline. We then form 90 interferograms between pair of SLC images whose acquisition dates is less than 1500 days apart and their perpendicular baseline (a parameter related to the orbital position of the satellite during the two acquisitions) is shorter than 2 km. The interferograms are then flattened using satellite ephemeris data and a Digital Elevation Model (DEM) with 30m resolution provided by the Shuttle Radar Topography Mission (SRTM) (Farr et al., 2007) to remove the effects of a flat earth and surface topography (Franceschetti & Lanari, 1999). The elite (i.e., less noisy) pixels are next identified using a statistical test, which investigates the time series of complex interferometric phase noise in the wavelet domain (Lopez-Martinez & Fabregas, 2002; Shirzaei, 2013). Next, the absolute estimates of the phase change associated with the identified elite pixels is obtained by applying an iterative three-dimensional phase unwrapping algorithm (Hooper & Zebker, 2007).

A set of wavelet-based filters are used to remove the nuisance signal associated with various sources of error in the unwrapped interferograms. The spatially correlated nuisance terms are mainly caused by the atmospheric delay and the orbital and satellite clock errors. To remove these errors, each

unwrapped interferogram is decomposed into its high-pass and low-pass sub-bands using a two-dimensional multiresolution wavelet transformation. The effect of residual orbital errors is removed by fitting a 2nd order polynomial to the average component (i.e., the high-pass sub-band) through a robust regression method (Shirzaei & Walter, 2011). On the other hand, the details coefficients (i.e., the low-pass sub-bands) are down-weighted according to their correlation with the corresponding details coefficients associated with the DEM of the study area to correct the interferogram for the phase contributions from the topography-correlated component of atmospheric delay (Shirzaei & Bürgmann, 2012). Moreover, the detail coefficients are further refined using a low-pass filter generated based on the Legendre polynomial wavelets to reduce the effect of residual DEM error, which appears as a high-spatial-frequency noise (Shirzaei, 2013).

The corrected unwrapped interferograms are then inverted using an iterative re-weighted least squares method (O'leary, 1990), where the weight of observation in each iteration changes based on the residuals from the previous iteration (Shirzaei, 2013), to obtain the deformation time series. Surface deformation rate at the location of elite pixels is then estimated as the slope of best-fitting line to the associated time series. Assuming all the deformation are vertical, the line-of-sight (LOS) observation is finally converted to the up-down direction using the LOS unit vector, which is a function of incidence angle at the location of elite pixels.

Supplement 2 – Full Poroelastic Solutions

Here, ΔP is the pressure change in the grid cell in the reservoir, vertices with index *i* referring to the vertices of the grid cell, $R_{\pm}=\left(\overline{x}^2+\overline{y}^2+\zeta_{\pm}^{\ 2}\right)^{\frac{1}{2}}$, $\zeta_{\pm}=z_i\pm z_{eval}$, $\overline{x}_i=x_i-x_{eval}$ etc., and x_{eval} denotes the location where the stress or displacement is evaluated.

$$\sigma_{xx}(x,t)=\Delta P\frac{\alpha C_m\mu}{2\pi}\sum_{vertices}(-1)^{i-1}¿¿$$

$$\sigma_{yy}(x,t)=\Delta P\frac{\alpha C_m\mu}{2\pi}\sum_{vertices}(-1)^{i-1}¿¿$$

534 $$\sigma_{zz}(x,t)=\Delta P\frac{\alpha C_m\mu}{2\pi}\sum_{vertices}(-1)^{i-1}¿¿$$

535 $$\sigma_{xy}(x,t)=-\Delta P\frac{\alpha C_m\mu}{2\pi}\sum_{vertices}(-1)^{i-1}¿¿$$

536 $$\sigma_{xz}(x,t)=\Delta P\frac{\alpha C_m\mu}{2\pi}\sum_{vertices}(-1)^{i-1}¿¿$$

537 $$\sigma_{yz}(x,t)=\Delta P\frac{\alpha C_m\mu}{2\pi}\sum_{vertices}(-1)^{i-1}¿¿$$

538 $$U_x(x,t)=\Delta P\frac{\alpha C_m}{4\pi}\sum_{vertices}(-1)^{i-1}¿$$

539 $$U_y(x,t)=\Delta P\frac{\alpha C_m}{4\pi}\sum_{vertices}(-1)^{i-1}¿$$

540 $$U_z(x,t)=-\Delta P\frac{\alpha C_m}{4\pi}\sum_{vertices}(-1)^{i-1}¿$$

541 $$f(x,y,Z,R)=Zatan\left(\frac{xy}{ZR}\right)-xln(R+y)-yln(R+x)$$

542

Supplement 3 – Supplemental Figures and Tables

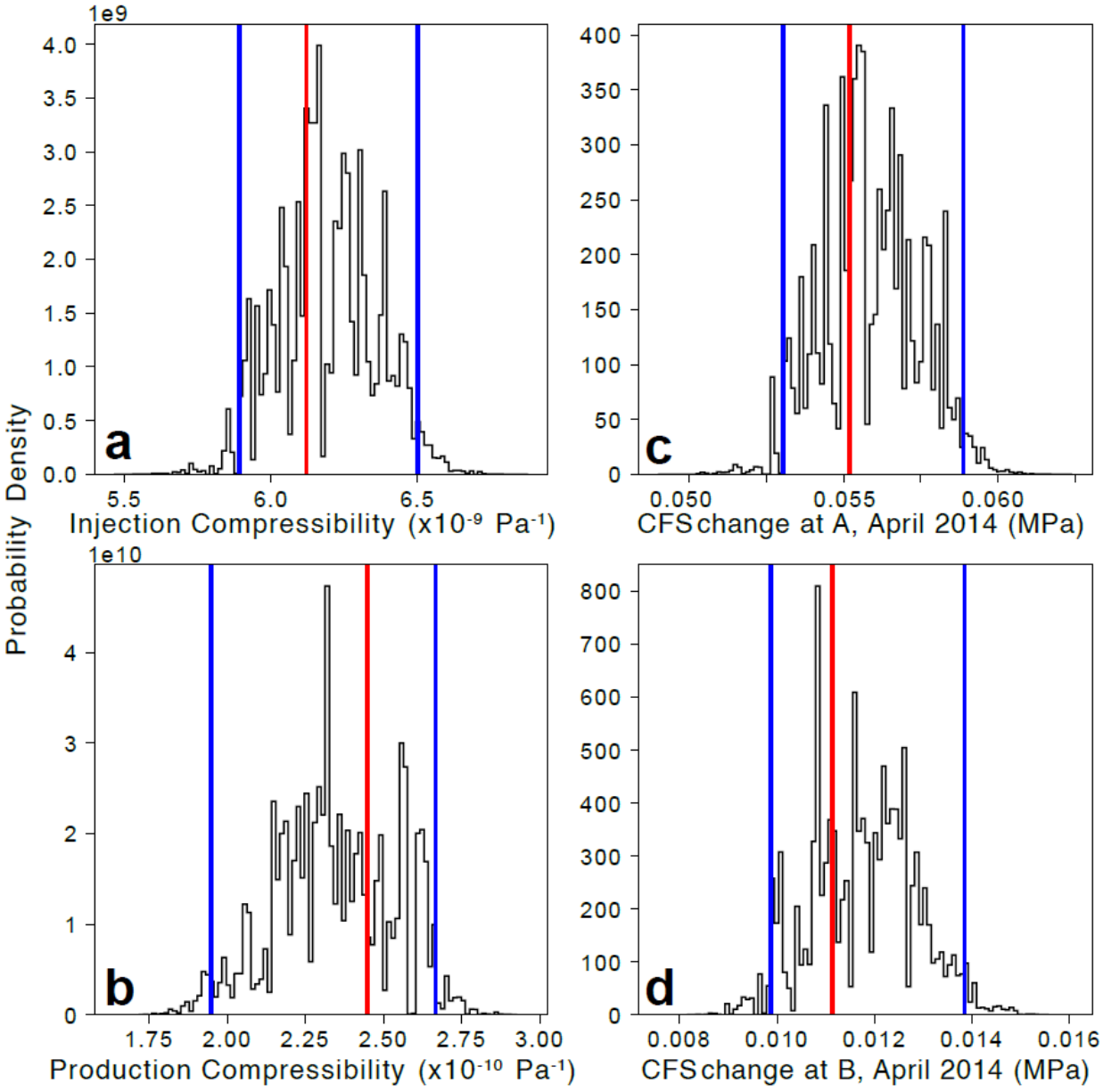

Figure S1: Results of 100,000 bootstrap samples each of size 10,000 to quantify model uncertainty. a) histogram of best-fit injection reservoir compressibility, b) histogram of best-fit production reservoir compressibility, c) histogram of best-fit Coulomb failure stress (CFS) change values at point "A" in Figure 1a, d) histogram of CFS change at point "B" Figure 3a. Red lines indicate overall best fit model, based on 1,000,000 generated samples, and blue lines indicate 2.5th and 97.5th percentiles denoting the 95% confidence range.

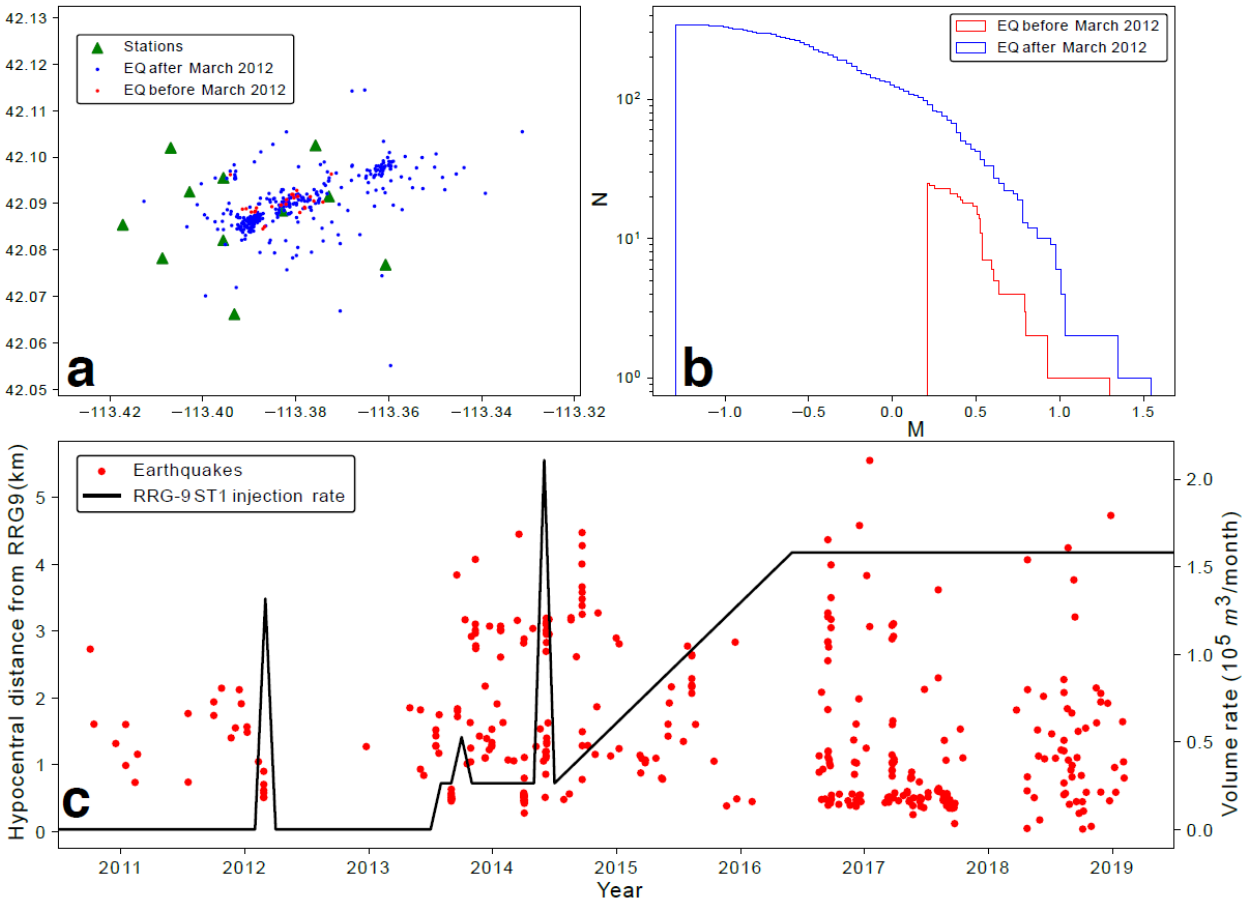

Figure S2: Summary plots showing a) location of seismicity before and after the first hydraulic stimulation in March 2012 alongside station locations, b) Frequency-Magnitude distribution of events, c) timing and distance of earthquakes relative to the RRG-9 wellhead.

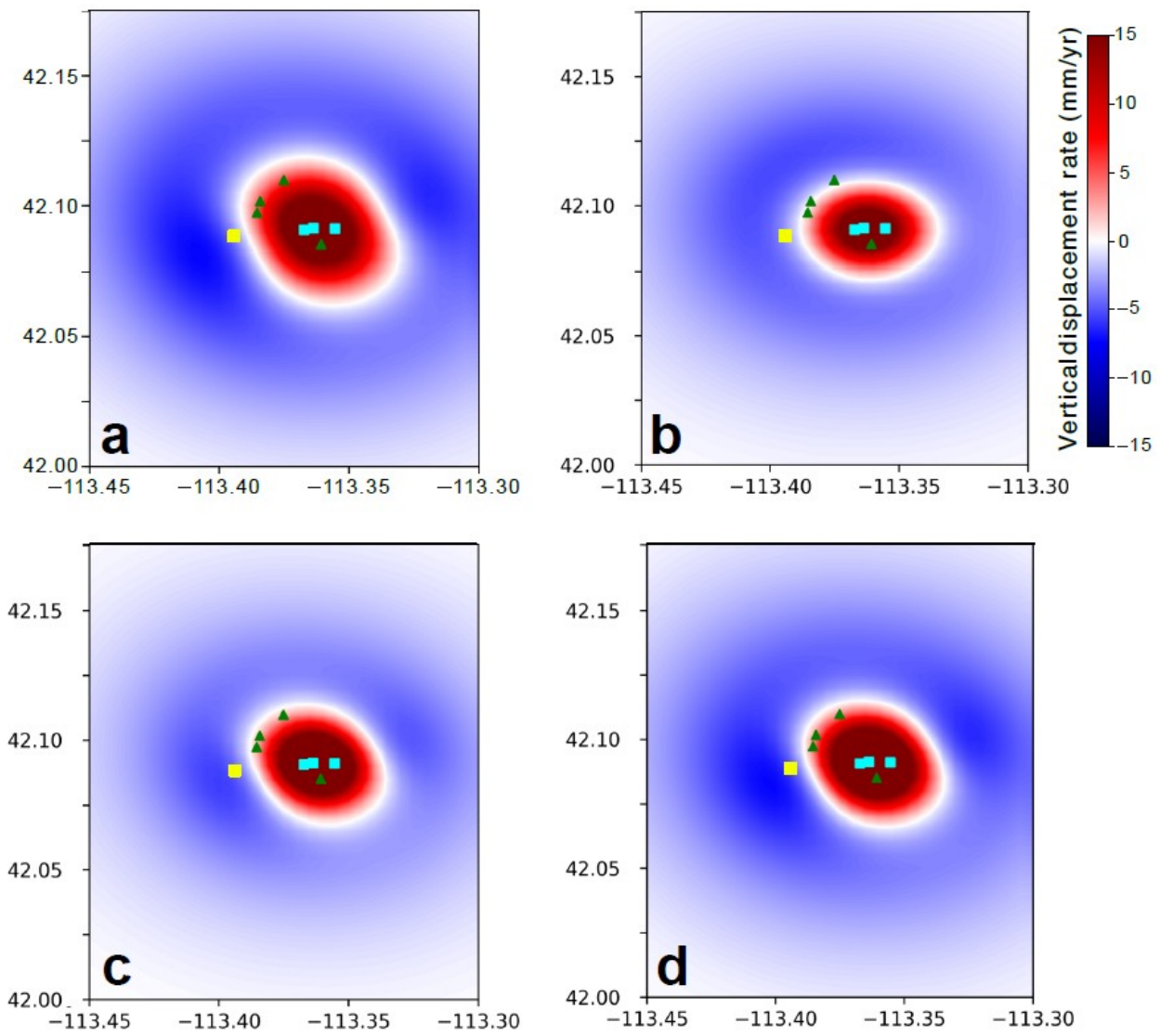

Figure S3: Comparison of modelled surface displacement from a) optimal model with anisotropy, b) isotropic model, c) model with injection reservoir permeability = 4.7 x 10^{-13} m^2, production reservoir permeability = 4 x 10^{-13} m^2, d) model with injection reservoir permeability = 7.1 x 10^{-13} m^2, production reservoir permeability = 6 x 10^{-13} m^2.

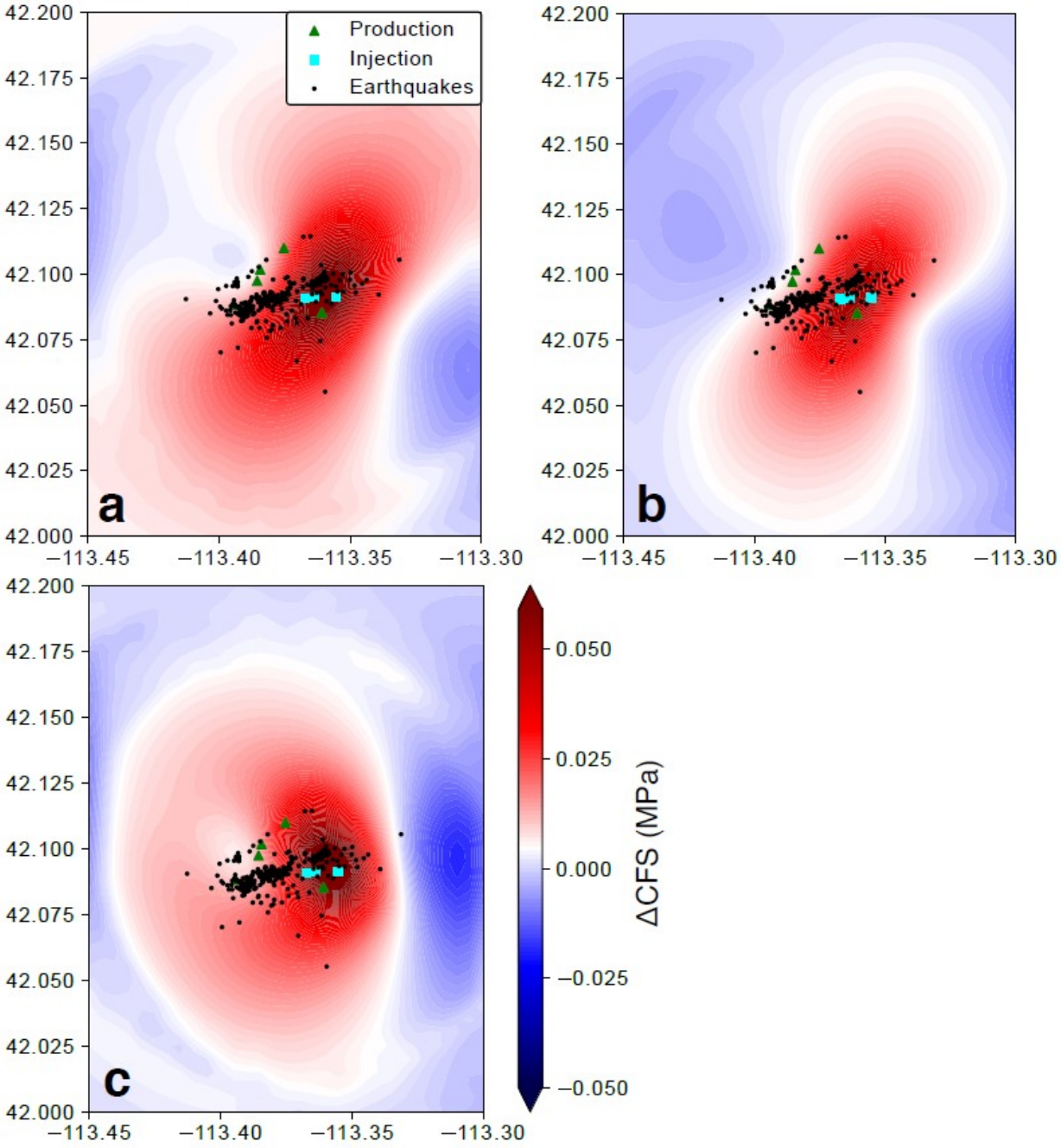

Figure S4: Comparison of effect of assumed fault plane (left-lateral N60E), a) shows model where CFS is calculated along the left-lateral N60E Narrows fault zone, b) model where CFS is calculated along left-lateral N-S striking faults, c) model where CFS is calculated along a normal-faulting N-S fault.